

¹ **Supplementary Information for**

² **A Statistical Dynamical Model to Predict Extreme Events and Anomalous Features in Shallow**
³ **Water Waves with Abrupt Depth Change**

⁴ **Andrew J. Majda, M. N. J. Moore, and Di Qi**

⁵ **This PDF file includes:**

⁶ Supplementary text
⁷ Figs. S1 to S7
⁸ Tables S1 to S2
⁹ References for SI reference citations

10 **Supporting Information Text**

11 **A. Details about the TKdV model non-dimensionalization**

12 We provide more details about the derivation and properties for the truncated KdV equation with abrupt depth change used as
13 the prediction model in the [main text](#). A unified formulation with dependence on different parameter values is provided.

14 **A.1. Mathematical formulation of the truncated KdV equation as a Hamiltonian system.** The classic *Korteweg-de Vries* (KdV)
15 equation (1) can be written in the standard form as

16
$$u_t + uu_x + u_{xxx} = 0, \quad x \in [-\pi L_0, \pi L_0]. \quad [1]$$

17 The state variable $u(x, t)$ for the leading-order surface wave disturbance is defined on a periodic geometry of length $2\pi L_0$. The
18 KdV equation [1] can be also recognized as a *Hamiltonian system* as

19
$$\dot{u} = \{u, \mathcal{H}\} = \mathcal{J} \frac{\delta \mathcal{H}}{\delta u}, \quad \mathcal{J} = -\partial_x, \quad \mathcal{H} = \int_{-\pi L_0}^{\pi L_0} \left(\frac{1}{6} u^3 - \frac{1}{2} u_x^2 \right) dx. \quad [2]$$

20 The Poisson bracket is defined by the symplectic operator \mathcal{J}

21
$$\{\mathcal{F}, \mathcal{G}\} = \int_{-\pi L_0}^{\pi L_0} \frac{\delta \mathcal{F}}{\delta u} \mathcal{J} \frac{\delta \mathcal{G}}{\delta u} dx,$$

22 which forms a skew-symmetric and bilinear form satisfying the Jacobi identity, $\{\{\mathcal{F}, \mathcal{G}\}, \mathcal{H}\} + \{\{\mathcal{H}, \mathcal{F}\}, \mathcal{G}\} + \{\{\mathcal{G}, \mathcal{H}\}, \mathcal{F}\} = 0$,
23 acting on functionals $\mathcal{F}(u)$ and $\mathcal{G}(u)$. The evolution of any functional $\mathcal{F}(u)$ obeys the dynamical equation

24
$$\mathcal{F}_t = \{\mathcal{F}, \mathcal{H}\}.$$

25 Immediately, we have the conservation of the Hamiltonian in [2], $\mathcal{H}_t = \{\mathcal{H}, \mathcal{H}\} = 0$. Besides the Hamiltonian \mathcal{H} , two other
26 important conserved quantities in the KdV equation are the momentum \mathcal{M} and energy \mathcal{E} defined as

27
$$\mathcal{M}(u) = \int_{-\pi L_0}^{\pi L_0} u dx, \quad \mathcal{E}(u) = \frac{1}{2} \int_{-\pi L_0}^{\pi L_0} u^2 dx.$$

28 In applications using the KdV equation for modeling water waves, it is useful to consider a normalized version of the
29 equation. For convenience, the total momentum is normalized to zero $\mathcal{M} = 0$ without loss of generality due to the Galilean
30 invariance and the total energy is rescaled to unity $\mathcal{E} = 1$. To achieve this, consider the following change of variables

31
$$t = \tilde{t}, \quad x = L_0 \tilde{x} + M_0 \tilde{t}, \quad u = E_0^{1/2} L_0^{-1/2} \tilde{u} + M_0,$$

32 where $M_0 = \int_{-\pi L_0}^{\pi L_0} u dx$ is the conserved total momentum and $E_0 = \frac{1}{2} \int_{-\pi L_0}^{\pi L_0} u^2 dx - \pi L_0 M_0^2$ is the conserved total energy from
33 the original system [1], and L_0 defines the characteristic length scale of the system. The additional shift in time $M_0 t$ in the
34 new coordinate creates the Doppler shift from the non-zero mean momentum M_0 . The *normalized KdV equation with zero*
35 *momentum and unit total energy* for the scaled state variable $\tilde{u}(\tilde{x}, \tilde{t})$ becomes

36
$$\tilde{u}_{\tilde{t}} + E_0^{1/2} L_0^{-3/2} \tilde{u} \tilde{u}_{\tilde{x}} + L_0^{-3} \tilde{u}_{\tilde{x} \tilde{x} \tilde{x}} = 0, \quad \tilde{x} \in [-\pi, \pi], \quad [3]$$

37 where the system is defined on the normalized periodic domain, and we have the normalized conservatives

38
$$\mathcal{M} = \int_{-\pi}^{\pi} \tilde{u} d\tilde{x} = 0, \quad \mathcal{E} = \frac{1}{2} \int_{-\pi}^{\pi} \tilde{u}^2 d\tilde{x} = 1.$$

39 The corresponding Hamiltonian functional becomes the difference between the cubic term H_3 and the quadratic term H_2

40
$$\tilde{\mathcal{H}}(\tilde{u}) = E_0^{1/2} L_0^{-3/2} H_3(\tilde{u}) - L_0^{-3} H_2(\tilde{u}), \quad H_3(\tilde{u}) = \frac{1}{6} \int_0^{2\pi} \tilde{u}^3 d\tilde{x}, \quad H_2(\tilde{u}) = \frac{1}{2} \int_0^{2\pi} \tilde{u}_{\tilde{x}}^2 d\tilde{x}. \quad [4]$$

41 Notice that the total momentum M_0 has no explicit contribution in the rescaled equation. E_0 is the total energy of the
42 system depending on the domain size L_0 , while $E_0 / (2\pi L_0)$ defines the energy density at unit scale length. The entire dynamics
43 of the equation is determined by setting the two parameters (E_0, L_0) . The choice of these parameter values will be discussed
44 next based on a proper non-dimensionalization of the physical model. The advantage of adopting the normalized formulation [3]
45 with Hamiltonian [4] is that it enables us to easily control the different cases with changing energy from a unified model setup.

46 **Truncated KdV equation on the spectral domain.** To investigate the turbulent dynamics generated from the KdV equation, usually a
 47 Galerkin projection \mathcal{P}_Λ is applied to the state variable u with a high wavenumber truncation up to Λ

48

$$u_\Lambda(x, t) \equiv \mathcal{P}_\Lambda u = \sum_{|k| \leq \Lambda} \hat{u}_k(t) e^{ikx}, \quad [5]$$

49 with in total $J = 2\Lambda + 1$ grid points. Accordingly, the truncated version of the KdV equation (TKdV) can be formulated by
 50 projecting the continuous equation [3] to the truncated subspace as

51

$$\frac{\partial}{\partial t} u_\Lambda + \frac{1}{2} E_0^{1/2} L_0^{-3/2} \frac{\partial}{\partial x} \mathcal{P}_\Lambda(u_\Lambda^2) + L_0^{-3} \frac{\partial^3}{\partial x^3} u_\Lambda = 0. \quad [6]$$

52 The additional projection in front of the quadratic term u_Λ^2 is used to remove the aliasing modes that go beyond the range
 53 $|k| > \Lambda$.

54 The TKdV equation [6] can be also written in the spectral domain for each Fourier mode \hat{u}_k as

55

$$\frac{d\hat{u}_k}{dt} = -\frac{ik}{2} E_0^{1/2} L_0^{-3/2} \sum_{|m| \leq \Lambda} \hat{u}_m \hat{u}_{m-k}^* + ik^3 L_0^{-3} \hat{u}_k.$$

56 It can be shown that the three conserved quantities above are still conserved in this truncated system. With the spectral
 57 representation, the conserved momentum and energy set the constraints on the spectral coefficients

58

$$\mathcal{M}_\Lambda = \int_0^{2\pi} u_\Lambda dx = (2\pi) \hat{u}_0 = 0, \quad \mathcal{E}_\Lambda = \frac{1}{2} \int_0^{2\pi} \mathcal{P}_\Lambda(u_\Lambda^2) dx = 2\pi \sum_{k=1}^{\Lambda} |\hat{u}_k|^2 = 1.$$

59 The discretized Hamiltonian can be written accordingly as

60

$$\mathcal{H}_\Lambda = E_0^{1/2} L_0^{-3/2} H_{3,\Lambda} - L_0^{-3} H_{2,\Lambda}, \quad H_{3,\Lambda} = \frac{\pi}{3} \sum_{|m|, |n| \leq \Lambda} \hat{u}_m \hat{u}_n \hat{u}_{m+n}^*, \quad H_{2,\Lambda} = \pi \sum_{|k| \leq \Lambda} k^2 |\hat{u}_k|^2.$$

61 Especially, the Hamiltonian structure of the previous continuous equation is maintained in this semi-discrete TKdV equation.
 62 The truncated equation [6] is still a Hamiltonian system with the corresponding discrete Hamiltonian \mathcal{H}_Λ . Furthermore, the
 63 truncated system [6] satisfies the Liouville property (2, 3), thus equilibrium statistical mechanics can be constructed based on
 64 the conserved quantities.

65 **A.2. The rescaled TKdV model with non-dimensionalized parameters.** Since the KdV equation is derived from the leading-
 66 order terms in the asymptotic expansion of the Euler equations, we find the sizes of the model parameters directly from the
 67 leading-order assumption for characterizing the physical problem from the experiments.

68 **The KdV equation with depth dependence.** The formulation for the KdV equation with a depth dependence D_0 can be introduced
 69 using the new coordinate system (X, ξ) for the convenience of derivation as

70

$$X = \epsilon x, \quad \xi = D_0^{-1/2} x - t. \quad [7]$$

71 The equation is used to describe the far-field and long-time variability at $X = O(1), \xi = O(1)$ as $x \rightarrow \infty$ and $t \rightarrow \infty$. With
 72 the water depth dependence, the leading-order wave disturbance $\eta(\xi, X)$ obeys the generalized KdV equation (derivation can
 73 be found in (1))

74

$$D_0^{1/4} \eta_X + \frac{3}{2} D_0^{-5/4} \eta \eta_\xi + \frac{1}{6} D_0^{3/4} \eta_{\xi\xi\xi} = 0. \quad [8]$$

75 It needs to be emphasized that the spatial variable X here plays the original role of the time variable t , and the new variable ξ
 76 tracks the right-moving waves along the characteristics in the new equation.

77 **Model parameters from non-dimensionalization.** To derive the model parameter values, we first propose scales in the state variables
 78 according to the dimensional formulation. Then the parameter values in the rescaled model can be found by comparing the
 79 equation with its non-dimensionalized version. For the basic scales in the problem, we consider: i) the typical depth of the
 80 water tank H_0 ; ii) the surface wave disturbance amplitude a ; and iii) the characteristic surface wavelength $\lambda_c = c_0/f_c$ with f_c
 81 the characteristic forcing frequency and the gravity wave speed $c_0 = \sqrt{gH_0}$. The important characterizing parameters that can
 82 be measured from the experiments include

83

$$\epsilon = \frac{a}{H_0}, \quad \delta = \frac{H_0}{\lambda_c}, \quad D_0 = \frac{d}{H_0}. \quad [9]$$

84 Above, ϵ is the wave amplitude to water depth ratio; δ is the water depth to wavelength scale ratio; and D_0 defines the
 85 normalized wave depth ratio in the depth change from $d = H_0$ to $d < H_0$. The interpretations and reference values of these
 86 model parameters are based on the experimental setup (4).

| $J = 32$ | | $\epsilon \in [0.0024, 0.024], \delta = 0.22, M = 5$ |
|----------|----------------|--|
| L_0 | | $2.0 - 6.3$ |
| E_0 | $\gamma = 1$ | 47.53 |
| | $\gamma = 0.5$ | 190.1 |
| D_0 | upstream | 1 |
| | downstream | 0.24 |

Table S1. Reference parameter values for the numerical model. The computation domain is set as $M = 5$ multiples of the characteristic wavelength.

We are interested in the surface waves at the limit $\epsilon \rightarrow 0, \delta \rightarrow 0$, so that the amplitude of the surface waves stays small and the shallow water approximation is valid. Then we introduce the characteristic physical scales for the surface disturbance η , spatial variable x , and temporal variable t , based on the scales in (1)

$$[\eta] = \epsilon H_0, [x] = \epsilon^{-1/2} H_0, [t] = \epsilon^{-1/2} H_0/c_0.$$

We use $(\eta; X, \xi)$ to represent the variables in the dimensional formulation [8]; and $(\tilde{u}; \tilde{t}, \tilde{x})$ for the final non-dimensionalized variables in [3]. The above scales give the relations between the two sets of variables

$$\tilde{u} = U^{-1} [\epsilon H_0] \eta, \tilde{x} = L_d^{-1} \left[\epsilon^{-\frac{1}{2}} D_0^{\frac{1}{2}} H_0 \right] \xi, \tilde{t} = L_s^{-1} \left[\epsilon^{-\frac{3}{2}} H_0 \right] X,$$

where (U, L_d, L_s) are the scales in (η, ξ, X) to normalize the original system to the standard form with unit energy and domain size 2π as in [3]. We introduce the length scale L_d according to the characteristic wavenumber λ_c and the spatial scale L_s according to slow-varying far-field variables

$$L_d = M \lambda_c = \frac{M \sqrt{gd}}{f_c}, \quad L_s = \epsilon^{-3/2} H_0 = \frac{\sqrt{H_0^5}}{\sqrt{a^3}}, \quad \gamma = \frac{U}{a} = \frac{U}{\epsilon H_0}. \quad [10]$$

where M is an integer representing a wave package of multiple wavelengths. Furthermore, γ defines the additional ratio that normalizes the total energy in u to unit. Substituting the above relations into the equation [8], we find the final non-dimensionalized equation about $\tilde{u}(\tilde{t}, \tilde{x})$

$$\frac{\partial \tilde{u}}{\partial \tilde{t}} + \epsilon^{-\frac{1}{2}} \frac{3\delta}{4\gamma M} D_0^{-\frac{3}{2}} \frac{\partial}{\partial \tilde{x}} (\tilde{u}^2) + \epsilon^{-\frac{3}{2}} \frac{\delta^3}{6M^3} D_0^{\frac{1}{2}} \frac{\partial^3 \tilde{u}}{\partial \tilde{x}^3} = 0. \quad [11]$$

Therefore, we formulate the non-dimensional equations [11] based on the non-dimensional parameters [9].

In the final step, we determine the parameter values in the computational models [3] by comparing with the corresponding non-dimensionalized form [11] with the measured quantities. After proper rearrangement and leaving the tildes in the normalized variables, we find the *normalized KdV equation* (as eqn. [1] in the [main text](#))

$$u_t + E_0^{1/2} L_0^{-3/2} D_0^{-3/2} u u_x + L_0^{-3} D_0^{1/2} u_{xxx} = 0, \quad x \in [-\pi, \pi], \quad [12]$$

The model parameters are determined by the non-dimensional measurements

$$L_0 = 6^{\frac{1}{3}} \left(M \epsilon^{\frac{1}{2}} \delta^{-1} \right), \quad E_0 = \frac{27}{2} \gamma^{-2} \left(M \epsilon^{\frac{1}{2}} \delta^{-1} \right). \quad [13]$$

Notice that in the above model ‘ t ’ is used to represent either the far-field spatial variable ‘ X ’ and ‘ x ’ is used to represent the wave location variable ‘ ξ ’. We also drop the ‘tildes’ in the variables for simplicity.

In addition, to estimate the parameter M for the computational domain size $2\pi L_d = 2\pi M \lambda_c$ determined as M -multiple of the characteristic wavelength λ_c , we consider the spatial discretization $J = 2\Lambda + 1 = 32$ so that the smallest resolved scale is comparable with the characteristic wavelength, that is, $2\pi M \lambda_c / J = \lambda_c$. This estimation gives $M = \frac{J}{2\pi} \sim 5$, inferring a computational domain with 5 multiples of the characteristic wavelength. Using the reference experimental measurements, we can calculate the reference values for the model scales L_0 and E_0 used in the direct numerical simulations. The wave amplitude to depth ratio ϵ changes in the range $[0.0024, 0.024]$, thus we can estimate the minimum and maximum values of the scales in Table S1. We adopt this basic guideline in choosing parameter values in the numerical confirmation of the theory in the [main text](#).

119 **B. Sampling strategy and statistical link for the invariant measures**

120 Here we show the detailed strategy and algorithm used for computing the sampled Gibbs invariant measure and the statistical
 121 matching at the abrupt depth change shown in the [main text](#). The invariant Gibbs measure is defined based on microcanonical
 122 ensemble in the quadratic energy \mathcal{E}_Λ on the isosurface and canonical ensemble in the Hamiltonian \mathcal{H}_Λ ([3](#), [5](#)). The *invariant*
 123 *Gibbs measure* for the TKdV model [[12](#)] about the normalized state variable u_Λ with unit energy can be written explicitly as

$$124 \quad \mathcal{G}_{\theta^\pm}(u_\Lambda) = C_{\theta^\pm} \exp \left(-\theta^\pm \left\{ h_3^\pm \sum_{1 \leq |m|, |n| \leq \Lambda} \hat{u}_m \hat{u}_n \hat{u}_{m+n}^* - h_2^\pm \sum_{1 \leq |k| \leq \Lambda} k^2 |\hat{u}_k|^2 \right\} \right) \delta \left(\pi \sum_{1 \leq |k| \leq \Lambda} |\hat{u}_k|^2 - 1 \right), \quad [14]$$

125 with the coefficients $h_3^\pm = \frac{\pi}{3} E_0^{1/2} L_0^{-3/2} D_\pm^{-3/2}$ and $h_2^\pm = \pi L_0^{-3} D_\pm^{1/2}$ depending on the model parameters. The proper statistical
 126 matching condition is proposed to connect the invariant measures in incoming and outgoing flow statistics with different inverse
 127 temperatures θ^\pm .

128 In predicting the statistical distribution of state variables after the abrupt depth change, we start with the assumption
 129 that we have full knowledge about the invariant distribution about the incoming flow field, \mathcal{G}_{θ^-} at equilibrium. Thus the
 130 parameters for θ^- are determined with accuracy from the observations or statistical simulations in the incoming flow, and the
 131 total energy E_0 is conserved. The condition to get the outgoing flow statistics with parameter θ^+ is through the following
 132 matching condition

$$133 \quad \langle H_\Lambda^+ \rangle_{\mathcal{G}_{\theta^-}} = \langle H_\Lambda^+ \rangle_{\mathcal{G}_{\theta^+}}, \quad [15]$$

134 with the Gibbs measures \mathcal{G}_{θ^\pm} before and after the abrupt depth change defined in [[14](#)]. Notice in the statistical matching
 135 condition [[15](#)], we don't require the statistical information for the incoming Hamiltonian H_Λ^- . This is considering the near-
 136 Gaussian statistics in the incoming waves and its weak dependence on the Hamiltonian in the Gibbs measure. Therefore the
 137 Hamiltonian before the depth change is only used to construct the invariant measure, \mathcal{G}_{θ^-} .

138 **B.1. Sampling algorithm for the incoming Gibbs measure.** First, the task is to compute the expectations $\langle H_\Lambda^+ \rangle_{\mathcal{G}_{\theta^\pm}}$ under
 139 the proper invariant measures from [[14](#)]. The central question is how to find a method to properly sample the equilibrium
 140 distribution according to the chosen inverse temperature θ . One method to directly sample the Gibbs measure is described in
 141 ([2](#)), where a Metropolis-Hastings Monte-Carlo sampling is applied. The following algorithm is adopted to sample the mixed
 142 canonical-microcanonical ensemble distribution [[14](#)] for the numerical results in the [main text](#):

Algorithm 1 Metropolis-Hastings sampling for the mixed ensemble for $\{\hat{u}_k\}_{k=1}^\Lambda$

- 1: Assign i.i.d standard Gaussian random variables to the Λ -dimensional complex valued samples, $\vec{w} = \{\hat{w}_1, \dots, \hat{w}_\Lambda\} \in \mathbb{C}^\Lambda$;
 - 2: Normalize for each component $\hat{u}_k = \sqrt{\frac{1}{E}} \hat{w}_k$ with the total energy $E = 2\pi \sum_{k=1}^\Lambda |\hat{u}_k|^2$;
 - 3: Starting from $\vec{u}_t = \vec{u}$, generate a new candidate \vec{w}' according to a transition probability, $g(\vec{w}' | \vec{u})$ (a simple choice is $g \sim \exp(-\frac{\Lambda}{2} |\vec{w} - \vec{u}|^2)$), and normalize $\vec{u}' \leftarrow \sqrt{\frac{1}{E}} \vec{w}'$;
 - 4: Calculate the acceptance probability $a = \min \left\{ 1, \exp(-\theta [H(\vec{u}') - H(\vec{u})]) \frac{g(\vec{u}' | \vec{u}')}{g(\vec{u}' | \vec{u})} \right\}$;
 - 5: Generate a uniform random number $r = \mathcal{U}[0, 1]$. Accept $\vec{u}_{t+1} = \vec{u}'$ if $r \leq a$ and reject $\vec{u}_{t+1} = \vec{u}$ if $r > a$;
 - 6: Repeat the previous steps and sample at every $n = 10$ steps.
-

142 We normalize the vector at each step to keep it on the fixed energy surface. It is also safer in practice to skip the first
 143 $M = 10^3$ samples from the start for the system to reach stationary. Then the expectations can be calculated by averaging
 144 among all the samples from the above algorithms

$$146 \quad \langle H_\Lambda^+ \rangle_\mu = \frac{1}{N} \sum_{t=1}^N H_\Lambda^+(\vec{u}_t) = E_0^{1/2} L_0^{-3/2} D_+^{-3/2} \frac{1}{N} \sum_{t=1}^N H_3(\vec{u}_t) - L_0^{-3} D_+^{1/2} \frac{1}{N} \sum_{t=1}^N H_2(\vec{u}_t),$$

147 where $H_3(\vec{u})$ computes the cubic term u^3 and $H_2(\vec{u})$ computes the wave slope energy u_x^2 according to the definition in [[2](#)].
 148 The PDFs are achieved by “bin counting” from the histogram of the samples $\{\vec{u}_t\}_{t=1}^N$. As one illustration, Figure S1 displays
 149 the sampled statistics, the PDFs for the Hamiltonian H_Λ , the PDFs for the state variable u_Λ , and the corresponding energy
 150 spectra for each Fourier mode. Typically we test the range of values of the inverse temperature from positive to negative
 151 $\theta = 0.5, 0.25, 0, -0.25, -0.5$. Supporting the claim in the [main text](#), the negative inverse temperature $\theta < 0$ produces the proper
 152 physical regime for the incoming flow statistics, where the energy spectrum is decaying from larger scale to small scale. In
 153 contrast with $\theta > 0$, the small scale modes get more energetic and a flat top is generated in the PDF of u_Λ with two peaks.
 154 With $\theta = 0$, the Gibbs measure is the uniform distribution on the constant energy shell E_0 , thus equipartition of energy in each
 155 mode is expected.

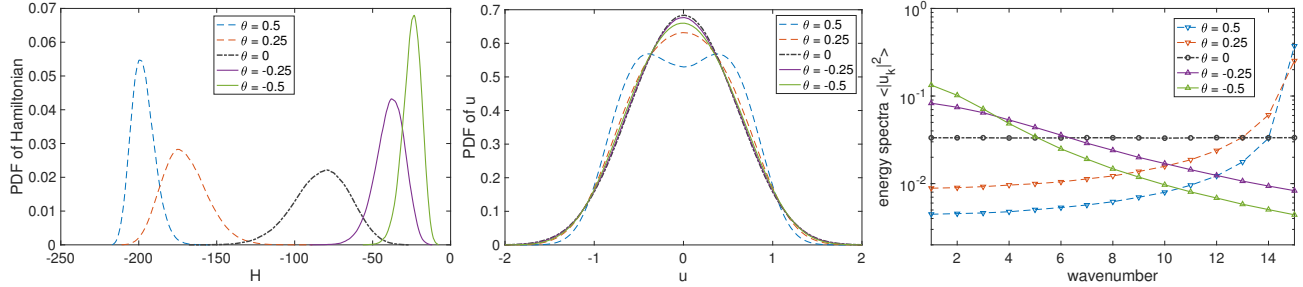


Fig. S1. Statistics generated from the Gibbs invariant measures with different inverse temperatures \$\theta\$ and \$D_0 = 1\$. Positive values of \$\theta\$ are shown in dashed lines and negative values of \$\theta\$ in solid lines.

156 **B.2. Computing downstream parameter from the statistical matching.** In the second step, we need to enforce the the statistical
157 matching condition [15] to discover the corresponding downstream inverse temperature \$\theta^+\$. For the efficiency of the method in
158 finding the optimal value of \$\theta_*^+\$, we use a secant method by solving a nonlinear equation following the algorithm:

Algorithm 2 Recovering the downstream inverse temperature \$\theta^+\$ from the statistical matching condition

- 1: Pick up the upstream value of \$\theta^-\$ and compute the expectation under incoming flow Gibbs measure \$\langle H_\Lambda^+ \rangle_{\mathcal{G}_{\theta^-}}\$;
 - 2: Define a function of \$\theta^+\$ as the difference of the upstream and downstream expectations, \$F(\theta^+) = \langle H_\Lambda^+ \rangle_{\mathcal{G}_{\theta^+}} - \langle H_\Lambda^+ \rangle_{\mathcal{G}_{\theta^-}}\$;
 - 3: Find the solution of \$F(\theta^+) = 0\$ using the secant method, so that the optimal downstream value \$\theta_*^+\$ is found.
-

159 In addition, to remove stiffness with large values of \$L_0\$ and \$E_0\$, we introduce the normalized parameter \$\tilde{\theta} = L_0^{-3/2}\theta\$ so that
160 \$\mathcal{G}_{\tilde{\theta}} \sim \exp(-\tilde{\theta} [E_0^{1/2} D_0^{-3/2} H_3 - L_0^{-3/2} D_0^{1/2} H_2])\$. In the numerical computations, we tune the parameter \$\tilde{\theta}\$ instead for the
161 matching condition. Using this modified secant method, it is found that the optimal value can be usually reached after 2 to 5
162 iteration steps as long as the scheme is guaranteed non-stiff.

163 **Numerical comparison of the matching results.** The solid black lines in Figure S2 plot the downstream skewness \$\kappa^+\$ computed
164 according to the matched downstream \$\theta^+\$ as shown in Fig. 1 of the [main text](#). Here as a further comparison, the results
165 with different total energy levels \$E_0\$ starting from various various values of incoming \$\theta^-\$ are compared. Further, Table S2
166 compares the incoming (with \$\theta^-\$) and outgoing (with \$\theta^+\$) wave statistics using the parameters achieved from the statistical
167 matching condition. In the last two rows, the contributions of the cubic term \$H_3\$ and quadratic term \$H_2\$ in the Hamiltonian
168 are compared in the incoming and outgoing flow statistics. It is found that in the upstream statistics \$\theta^-\$, the quadratic part
169 \$H_2\$ is dominant, while in the downstream flow statistics, the cubic part becomes important in the total Hamiltonian, implying
170 stronger non-Gaussian statistics.

171 As a further comparison, in the [main text](#) we also use the Gamma distribution

$$172 \rho(u; k, \alpha) = \frac{e^{-k} \alpha^{-1}}{\Gamma(k)} (k + \alpha^{-1} u)^{k-1} e^{-\alpha^{-1} u}, \quad \sigma^2 = k\alpha^2, \quad \kappa_3 = \frac{2}{\sqrt{k}},$$

173 to fit the downstream state \$u^+\$ according to the measured skewness \$\kappa_3\$ and variance \$\sigma^2\$ for the parameters \$(k, \alpha)\$. Table S2
174 also shows the fitting parameter values according to the downstream statistics with \$\theta^+\$. The Gamma fitting can also give an
175 estimation for the kurtosis as \$\kappa_4 = \frac{6}{k} + 3\$, which is shown to have good agreement with the truth value \$\kappa_4^+\$ especially in the
176 larger skewness cases.

177 **An explicit formula from the statistical matching condition.** In complementary to the [main text](#), we offer a more detailed derivation
178 about the statistical link between the upstream and downstream wave slope energy and the skewness. The statistical matching
179 condition with the downstream Hamiltonian can be written as

$$180 \langle H_\Lambda^+ \rangle_{\mu_-} = \langle H_\Lambda^+ \rangle_{\mu_+}, \quad H_\Lambda^+ = E_0^{1/2} L_0^{-3/2} D_+^{-3/2} H_3 - L_0^{-3} D_+^{1/2} H_2.$$

181 In general, we can have the expected value of \$H_3\$ and \$H_2\$ about any probability measure \$\mu\$ as

$$182 \langle H_3 \rangle_\mu = \frac{1}{6} \int_0^{2\pi} \langle u^3 \rangle_{\mu_-} dx = \frac{2\pi}{6J} \sum_{j=1}^J \langle u_j^3 \rangle_\mu, \quad \langle H_2 \rangle_\mu = \frac{1}{2} \int_0^{2\pi} \langle (u_x)^2 \rangle_\mu dx = \frac{2\pi}{2} \sum_{|k|=1}^\Lambda k^2 \langle |\hat{u}_k|^2 \rangle_\mu.$$

183 Above the quadratic term \$H_2\$ characterizes the *slopes of the surface waves*, \$u_x\$, in the incoming and outgoing flows. Beside, the
184 skewness the state variable \$u\$ at one grid point is defined as the ratio between the third and second moments (note that in the

| θ^- | $E_0 = 100$ | -0.5 | -0.3 | -0.1 |
|---|---------------|-------------|--------------|---------------|
| θ^+ | | -0.32 | -0.26 | -0.12 |
| $\langle H_\Lambda^+ \rangle_{\theta^-} = \langle H_\Lambda^+ \rangle_{\theta^+}$ | | -9.57 | -15.72 | -28.17 |
| κ_3 | θ^- | 0.16 | 0.093 | 0.024 |
| | θ^+ | 0.85 | 0.62 | 0.24 |
| κ_4^+ | | 3.96 | 3.42 | 2.88 |
| Gamma | (k, α) | (5.5, 0.24) | (10.4, 0.18) | (68.0, 0.068) |
| fitting | $6/k + 3$ | 4.08 | 3.58 | 3.08 |
| $\langle \tilde{H}_3 \rangle_\theta$ | θ^- | 0.31 | 0.17 | 0.043 |
| | θ^+ | 13.64 | 9.92 | 3.85 |
| $\langle \tilde{H}_2 \rangle_\theta$ | θ^- | 24.85 | 35.09 | 58.25 |
| | θ^+ | 23.38 | 25.73 | 32.58 |

Table S2. Statistics computed from incoming and outgoing flow Gibbs measures with $E_0 = 100$. The skewness κ_3 and kurtosis κ_4 predicted from the Gibbs measures with different θ^- are compared. The outgoing statistics are compared with the Gamma function fitting with parameter (k, α) and the corresponding kurtosis $\kappa_4 = 6/k + 3$. The expected values of the cubic and quadratic terms in the Hamiltonian, $\tilde{H}_3 = E_0^{1/2} L_0^{-3/2} D_\pm^{-3/2} \frac{1}{6} \int u^3$, and $\tilde{H}_2 = L_0^{-3} D_\pm^{1/2} \frac{1}{2} \int u_x^2$ are also compared.

185 homogeneous model setup, we always have zero mean in the state variable $\langle u \rangle \equiv 0$)

$$186 \quad \kappa_3 = \frac{\langle u_j^3 \rangle_\mu}{\langle u_j^2 \rangle_\mu^{\frac{3}{2}}}, \quad \frac{1}{2} \int_0^{2\pi} \langle u^2 \rangle_\mu dx = \frac{2\pi}{2J} \sum_{j=1}^J \langle u_j^2 \rangle_\mu = 1.$$

187 Above the total energy of the system is normalized to one in the computations. Now we use the two assumptions introduced in
188 the main text:

- 189 • The upstream equilibrium measure μ_- has a near-Gaussian distribution, so that the third moments in the cubic term
190 stay in a small value

$$191 \quad \langle H_3 \rangle_{\mu_-} = \frac{1}{6} \int_0^{2\pi} \langle u^3 \rangle_{\mu_-} dx = \epsilon;$$

- 192 • The downstream equilibrium measure μ_+ is homogeneous at each physical grid point, so that the second and third
193 moments are invariant at each grid point

$$194 \quad \langle u_j^2 \rangle_{\mu_+} = \sigma^2 = \pi^{-1}, \quad \langle u_j^3 \rangle_{\mu_+} = \sigma^3 \kappa_3 = \pi^{-\frac{3}{2}} \kappa_3.$$

195 With the homogeneous assumption above, the downstream cubic term can be simplified as

$$196 \quad \langle H_3 \rangle_{\mu_+} = \frac{\pi}{3J} \sum_{j=1}^J \langle u_j^3 \rangle_{\mu_+} = \frac{1}{3} \pi^{-\frac{1}{2}} \kappa_3.$$

With the above assumptions, the above statistical matching condition can be simplified as

$$\begin{aligned} E_0^{1/2} L_0^{-3/2} D_+^{-3/2} \epsilon - L_0^{-3} D_+^{1/2} \langle H_2 \rangle_{\mu_-} &= E_0^{1/2} L_0^{-3/2} D_+^{-3/2} \langle H_3 \rangle_{\mu_+} - L_0^{-3} D_+^{1/2} \langle H_2 \rangle_{\mu_+} \\ \Rightarrow E_0^{1/2} L_0^{-3/2} D_+^{-3/2} \epsilon + \pi L_0^{-3} D_+^{1/2} \sum_{1 \leq |k| \leq \Lambda} k^2 (r_k^+ - r_k^-) &= \frac{1}{3} \pi^{-1/2} E_0^{1/2} L_0^{-3/2} D_+^{-3/2} \kappa_3, \end{aligned}$$

197 with $r_k^- = \langle |\hat{u}_k|^2 \rangle_{\mu_-}$ the variance in upstream statistics and $r_k^+ = \langle |\hat{u}_k|^2 \rangle_{\mu_+}$ the statistics from downstream statistics. Therefore
198 we can estimate the skewness of the state variable u from the energy spectra in inflow and outflow statistics

$$199 \quad \kappa_3^+ = 3\pi^{\frac{3}{2}} L_0^{-\frac{3}{2}} E_0^{-\frac{1}{2}} D_+^2 \sum_{1 \leq |k| \leq \Lambda} k^2 (r_k^+ - r_k^-) + 3\pi^{\frac{1}{2}} \epsilon. \quad [16]$$

200 With further assumption that the incoming flow gets zero third moment, then the skewness above can be calculated by

$$201 \quad \kappa_3^+ = C \sum_{1 \leq |k| \leq \Lambda} k^2 (r_k^+ - r_k^-), \quad C = 3\pi^{\frac{3}{2}} L_0^{-\frac{3}{2}} E_0^{-\frac{1}{2}} D_+^2,$$

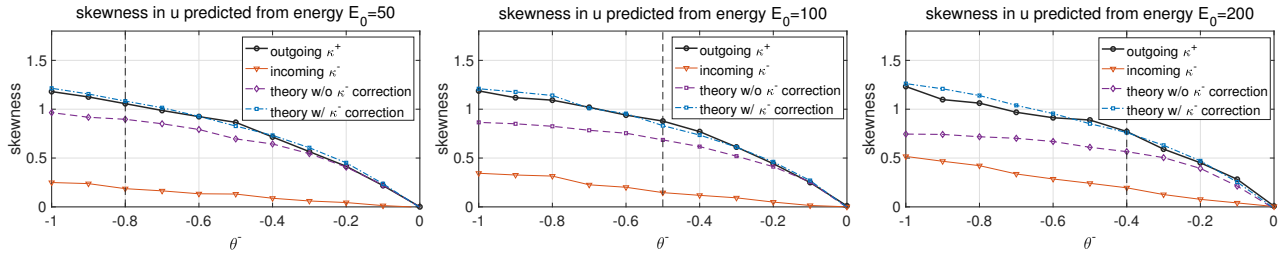


Fig. S2. Confirmation of the theoretical approximation of the skewness in the state u using energy in the wave slope u_x . The results with and without the incoming flow skewness correction κ_3^- are compared. The vertical line marks the value where the statistical matching condition is valid.

with the coefficient C depending on the model setup. Especially, we can see that a positive skewness can be generated from $r_k^+ > r_k^-$ in small scale modes and $r_k^+ < r_k^-$ in large scales. The total energy of the system is always normalized to unit, $\pi \sum r_k^+ = \pi \sum r_k^- = 1$.

Notice that in [16], the spectral difference between the incoming and outgoing flows

$$\sum_{1 \leq |k| \leq \Lambda} k^2 (r_k^+ - r_k^-) = \frac{1}{2\pi} \int_0^{2\pi} [\langle (u_x)^2 \rangle_{\mu_+} - \langle (u_x)^2 \rangle_{\mu_-}] dx,$$

calibrates the statistics in the ‘waves slopes’, u_x , before and after the depth change. Therefore, the skewness in the surface wave displacement statistics is connected with the waves slopes between the incoming and outgoing waves. This is consistent with the physical understanding in the flow field, since a stronger slope in the waves always implies the larger skewness in the disturbance.

In Figure S2, we compare the accuracy of the theoretical estimation derived above using numerical tests. In the regime with small incoming inverse temperature θ^- , the theoretical formula in [16] offers quite accurate approximation of the third-order skewness using only information from the second-order moments of the wave-slope spectrum. When θ^- grows larger in amplitude, the error without the incoming flow correction becomes large. The improvement is obvious by adding the correction from the incoming wave skewness κ^- . However, for the statistical matching condition, there exists a maximum amplitude threshold of θ^- for the matching to be valid (so that $\langle H^- \rangle$ stays negative). The maximum threshold value of θ^- is marked by the dashed vertical line.

C. Symplectic scheme for direct numerical simulations of the TKdV equation

Here we summarize the direct numerical methods used for the validation of the statistical theory in the [main text](#). In general, the strategy by using direct numerical simulations to confirm the anomalous statistics follows the steps:

1. Generate samples from the incoming equilibrium distribution μ_∞^- according to Algorithm 1 for the incoming waves. The model parameters (E_0, L_0, Λ) are determined from the experimental measurements and statistics in the incoming flow;
2. Compute the expectation of the outflow Hamiltonian, $\langle H_\Lambda^+ \rangle_{\mu_\infty^-}$, under the chosen incoming Gibbs measure $\mu_\infty^- = \mathcal{G}_{\theta^-}$;
3. The outgoing flow statistics can be predicted by both the equilibrium statistical mechanics and the direction model simulations.
 - (a) Equilibrium statistical mechanics: find the optimal outgoing flow parameter θ_*^+ from matching the expectation in [15] with the inflow value according to Algorithm 2. Then the new equilibrium distribution μ_∞^+ after the abrupt depth change can be sampled using the same method;
 - (b) Direct model simulations: run the dynamical model [12] with outflow depth $D_+ < 1$ starting from the state sampled from the inflow distribution \mathcal{G}_{θ^-} . The outgoing flow statistics can be captured by the solution from the direction simulations.

Above we proposed two approaches to predict the statistics in the downstream wave disturbance. The equilibrium statistical mechanics is an easy way to confirm the matching condition and get the equilibrium distribution in far-field long-time limit. On the other hand, the direct simulations of the dynamical model can offer estimates about the transient statistics before the far-field equilibrium state is reached. These two approaches can be used to confirm each other in the numerical results.

C.1. Conservation of energy and Hamiltonian form the symplectic scheme. For running the direct numerical simulations of the TKdV equations, a proper symplectic integrator is necessary to guarantee the conservation of the Hamiltonian and energy in time. As emphasized in the [main text](#), the conservation property plays a central role in the statistical matching and the final equilibrium measure, otherwise the non-symplectic schemes introduce high numerical dissipations. The symplectic scheme used here for the time integration of equation [12] is the 4th-order midpoint method (6). Let \mathbf{u}^n be the solution at time t_n and \mathbf{u}^{n+1}

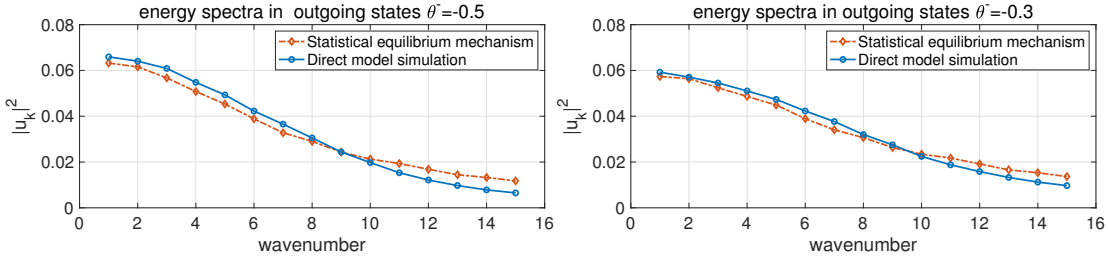


Fig. S3. Comparison of the energy spectra computed from directly running the numerical model and the energy spectra predicted from the Gibbs invariant measure in equilibrium statistical mechanics. The model simulations start with the Gibbs measure with different incoming flow parameter θ^- .

be the solution at next time step $t_{n+1} = t_n + \Delta t$, and \mathbf{F} the discretized operator for the spectral modes. The midpoint method has two intermediate stages and the auxiliary vectors $\mathbf{y}_1, \mathbf{y}_2$

$$\begin{aligned}\mathbf{y}_1 - \mathbf{u}^n &= w_1 \Delta t \mathbf{F} \left(\frac{1}{2} [\mathbf{y}_1 + \mathbf{u}^n] \right), \\ \mathbf{y}_2 - \mathbf{y}_1 &= w_2 \Delta t \mathbf{F} \left(\frac{1}{2} [\mathbf{y}_2 + \mathbf{y}_1] \right), \\ \mathbf{u}^{n+1} - \mathbf{y}_2 &= w_3 \Delta t \mathbf{F} \left(\frac{1}{2} [\mathbf{u}^{n+1} + \mathbf{y}_2] \right),\end{aligned}$$

with the time increments $w_1 = (2 + 2^{1/3} + 2^{-1/3}) / 3$, $w_2 = 1 - 2w_1$, and $w_3 = w_1$. Then the PDFs can be counted from the solution $u_\Lambda(t)$, and the statistical expectations can be calculated by averaging along the trajectory

$$\langle F(u_\Lambda) \rangle_\mu = \frac{1}{T} \int_{t_0}^{t_0+T} F(u_\Lambda(t)) dt,$$

given ergodicity in the solution with $u_\Lambda(t_0)$ already reaching the stationary state.

We compare the statistical spectra from the direct Monte Carlo model simulation with the prediction from the equilibrium statistical mechanics in Figure S3. The flow energy spectra computed both from the direct TKdV model simulations and from the Gibbs invariant measure in the equilibrium statistical mechanics are compared. Starting from two different θ^- initial states, the direct model simulations offer the final equilibrium energy spectrum in a comparable decaying structure as predicted from the Gibbs measure and statistical matching condition. This first comparison offers the consistency in these two distinct approaches.

C.2. Ergodicity and mixing properties in the TKdV solutions. Ergodicity is another crucial feature that needs to be confirmed in the TKdV equation solution. To achieve reasonable statistics from averaging the model time solutions, it is important to make sure that the solution is turbulent mixing. Following we display the direct numerical simulation solutions from the TKdV equation using initial states sampled from different inverse temperatures.

Mixing solutions starting from negative inverse temperature $\theta < 0$. In the [main text](#), the results shown always use negative inverse temperature. As shown from (2, 5) and Figure S1 before, this is a reasonable choice to generate a decaying energy spectrum. Here as a further illustration, we show that the negative inverse temperature case also generates fast mixing solutions to calculate reasonable statistical averages.

In Figure S4 and S5, we display the single trajectory solutions for both downstream $D_+ = 0.24$ and upstream $D_- = 1$ flows. The initial state is taken from the samples in Algorithm 1 with a negative initial temperature $\theta < 0$. The other parameters are kept the same as in the main text. On the left panel, the contour plot for the time-series of u_Λ is shown for the downstream and upstream flows. Both cases display turbulent dynamics, while the downstream solution with $D_+ < 0$ generates more rare events and stronger turbulence.

For more detailed comparison, the right panels show one slice of the time-series of $u_\Lambda(x_1)$ at one physical location as well as the first two Fourier modes, \hat{u}_1, \hat{u}_2 , in the spectral domain. The rare events in the downstream solution in Figure S4 are obvious with high peaks representing the generation of skewed PDFs in the positive direction. In comparison, the upstream solution in Figure S5 displays almost symmetric values in positive and negative disturbances, implying near-Gaussian statistics in the incoming flow. The mixing properties are characterized by the autocorrelation and decorrelation time of the state variable. The decorrelation time T_k and absolute decorrelation time T_k^{abs} together with the autocorrelation function \mathcal{R}_k in each spectral mode are defined as

$$T_k = \left| \int \mathcal{R}_k(t) dt \right|, \quad T_k^{\text{abs}} = \int |\mathcal{R}_k(t)| dt, \quad \mathcal{R}_k(t) = \langle \hat{u}_k(0) \hat{u}_k(t)^* \rangle / \langle |\hat{u}_k|^2 \rangle.$$

Decaying autocorrelations in both the physical state and the spectral modes confirm the fast mixing and turbulent dynamics in both the tested regimes used in the main text (though weaker in upstream). We can observe the much faster time scales in

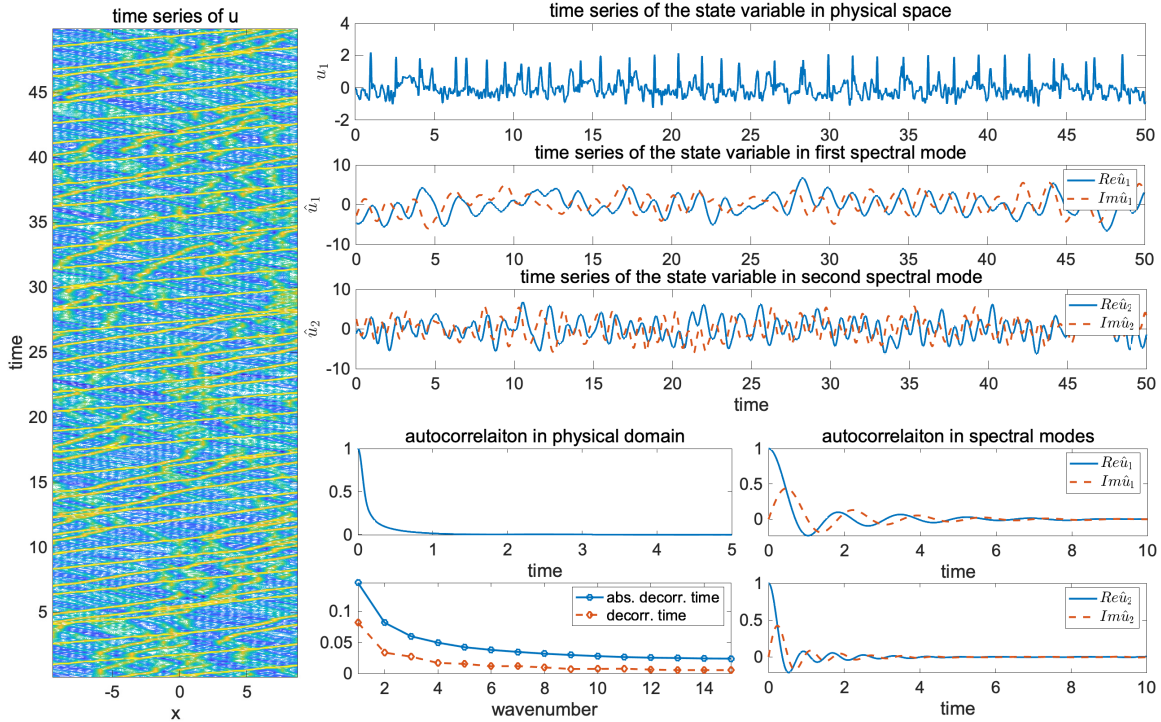


Fig. S4. Realization of the downstream flow solution with $D_0 = 0.24$ and initial state from samples with negative inverse temperature.

277 the downstream flow in the autocorrelation functions in the corresponding time-series. The longer decorrelation times in the
278 upstream flow indicate oscillating autocorrelations for a long time.

279 As an additional comparison, we show the power spectra of the upstream and downstream flows from the above test cases
280 in Figure S6. The power spectrum can be calculated by the Fourier transform of the autocorrelation function

$$281 \quad S(\lambda) = \int_{-\infty}^{\infty} \mathcal{R}(\tau) e^{-i\lambda\tau} d\tau,$$

282 which offers the characterization of the decay in power at each time frequency. Again, consistent with the observations from
283 experiments (4) and the numerics in the [main text](#), the downstream power spectrum gets more energetic small time scales at
284 low frequency modes and a slower decay rate in the high frequency modes compared with the upstream case. Also notice that
285 the peak in the incoming flow power spectrum is taken place at a much lower frequency. This illustrates the slower mixing rate
286 in the incoming flow state.

287 **Non-mixing solutions starting from positive inverse temperature $\theta > 0$.** In comparison, we also compute the solution starting from an
288 initial state with a positive inverse temperature $\theta > 0$. In contrast to the previous case in Figure S5, the only difference in
289 the present case is the initial state taken from the samples in an invariant measure with positive inverse temperature. Figure
290 S7 displays the corresponding solution in this $\theta > 0$ case. In contrast to the previous mixing solution with negative inverse
291 temperature, drastic difference performance is generated due to only the change in the initial state. The solution is recurrent
292 in time with interacting small scales. As a result, the solution in stationary waves lacks the proper mixing property and the
293 autocorrelation just oscillates for an extremely long time.

294 Accordingly in the autocorrelation functions and decorrelation times, the autocorrelation functions just keep oscillating and
295 all the modes get long absolute decorrelation time (the decorrelation time is small due to the cancellation from the oscillations).
296 This non-mixing feature with positive temperature supports the conclusion in the main text that this regime is not appropriate
297 for correctly representing the physical statistics in the experimental setups. This simple test further confirms the unrealistic
298 energy spectra in the positive temperature case with increasing energy in the smaller scales shown in (5) and Figure S1.

299

300 References

- 301 1. Johnson RS (1997) *A modern introduction to the mathematical theory of water waves*. (Cambridge university press) Vol. 19.
- 302 2. Abramov RV, Kovačić G, Majda AJ (2003) Hamiltonian structure and statistically relevant conserved quantities for the
303 truncated burgers-hopf equation. *Communications on Pure and Applied Mathematics: A Journal Issued by the Courant
304 Institute of Mathematical Sciences* 56(1):1–46.

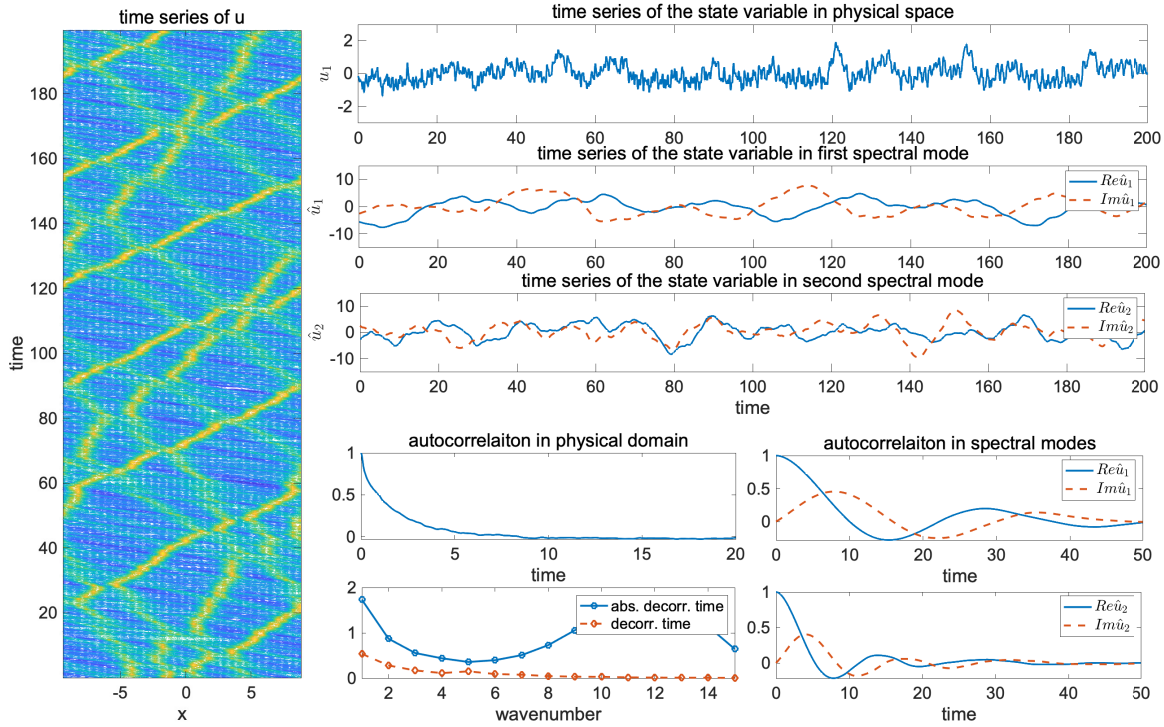


Fig. S5. Realization of the upstream flow solution with $D_0 = 1$ and initial state from samples with negative inverse temperature.

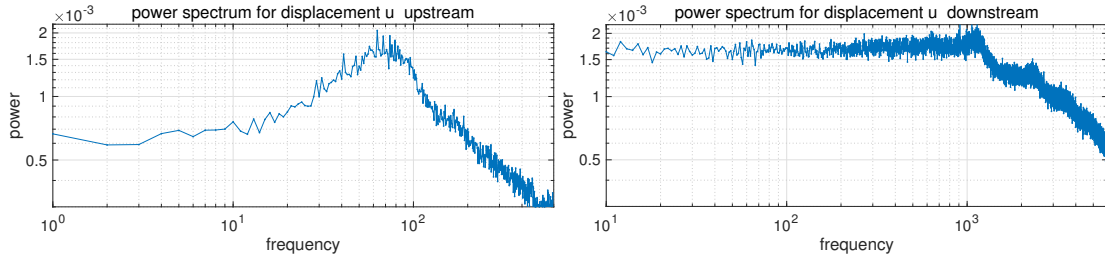


Fig. S6. Power spectra of the upstream and downstream states u_A .

- 305 3. Majda A, Wang X (2006) *Nonlinear dynamics and statistical theories for basic geophysical flows*. (Cambridge University
306 Press).
307 4. Bolles CT, Speer K, Moore M (2018) Anomalous wave statistics induced by abrupt depth change. *arXiv preprint*
308 *arXiv:1808.07958*.
309 5. Bajars J, Frank J, Leimkuhler B (2013) Weakly coupled heat bath models for gibbs-like invariant states in nonlinear wave
310 equations. *Nonlinearity* 26(7):1945.
311 6. McLachlan R (1993) Symplectic integration of hamiltonian wave equations. *Numerische Mathematik* 66(1):465–492.

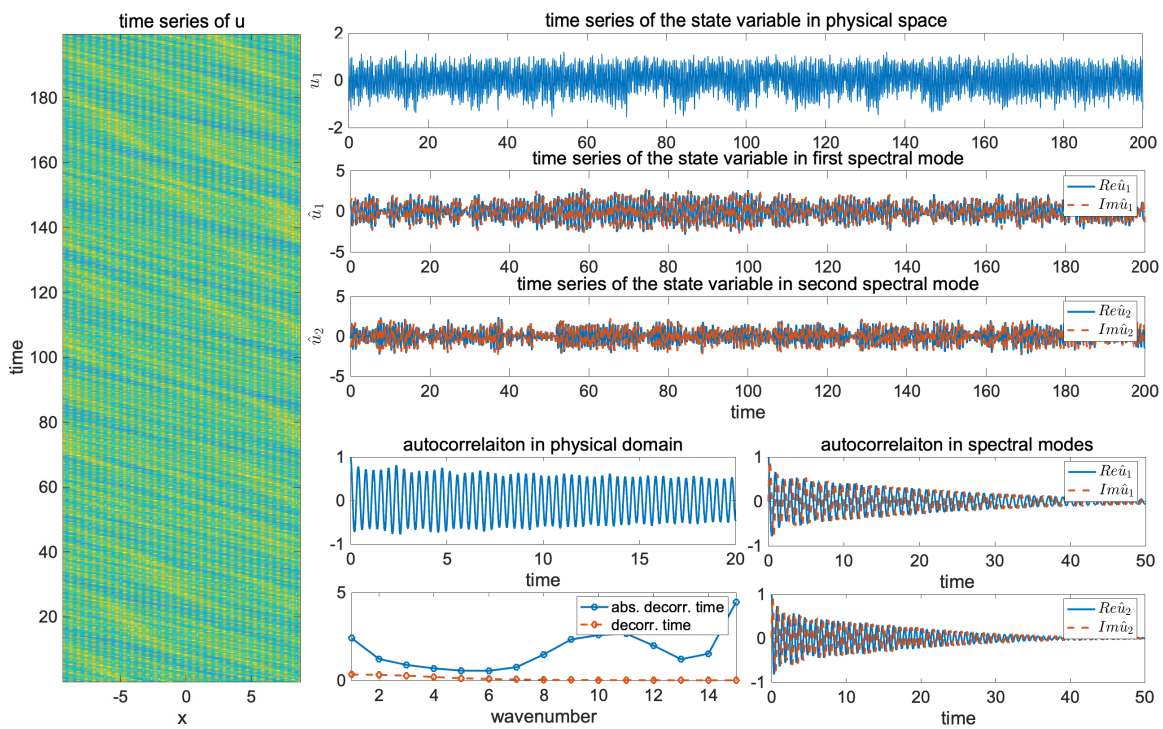


Fig. S7. Realization of the upstream flow solution with $D_0 = 1$ and initial state from samples with positive inverse temperature.